Periodically plunging foil near a free surface

D.J. Cleaver, D.E. Calderon, Z. Wang, and I. Gursul
Department of Mechanical Engineering
University of Bath, BA2 7AY, UK

Abstract

Experiments were performed to investigate the effects of amplitude and depth on the drag reduction of a NACA 0012 airfoil plunging near a free surface for a range of frequencies. Beyond the effect of the free surface, at low Strouhal numbers based on amplitude, Sr_A, the drag reduction follows a parabolic trend with greater effect for greater amplitude, similar to the Garrick predictions. At $Sr_A \approx 0.08$ larger amplitudes break from this trend due to leading-edge vortex formation. As a result smaller amplitudes become preferable for $Sr_A > 0.12$. In addition, for the first time vortex lock-in is documented experimentally. The effect of depth is twofold, firstly with decreasing depth there is a general departure from the Garrick trends. Secondly, a reduction in thrust is observed around a constant unsteady parameter of $\tau = U_\infty 2\pi f/g \approx 0.25$; around this value significant free surface waves form that detract from thrust creation. For depths greater than two chord lengths, there is negligible free surface effect.

List of Symbols

a	Amplitude of plunging motion
A	Peak to peak amplitude of plunging motion
C_d	Time-averaged drag coefficient
C_{d0}	Time-averaged drag coefficient for the stationary foil
c	Chord length
d	Depth
f	Frequency
h	Foil position
Fr	Froude number, $U_\infty/\sqrt{gc}$
Re	Reynolds number, $\rho U_\infty c/\mu$
Sr_c	Strouhal number based on chord, fc/U_∞
Sr_A	Strouhal number based on amplitude, $2fa/U_\infty$
t	Time, t = 0 is top of motion
T	Plunge period
U_∞	Free stream velocity
α	Angle of attack
λ_w	Wavelength of water wave
μ	Viscosity
ρ	Density
τ	Unsteady parameter, $U_\infty 2\pi f/g$

1 Introduction

There is currently the demand for naval vessels to go faster, more efficiently. To achieve this it will be necessary to use some form of drag reduction. Promising technologies based on injection of microbubbles (McCormic and Bhattach 1973; Shen et al. 2006) and polymers (Winkel et al. 2009) into the boundary layer have been developed in laboratory tests for stationary surfaces and foils. Although these technologies have demonstrated great potential for drag reduction (as much as 80%) at low speeds and for stationary surfaces, they are not proven for realistic conditions where the vessel motion is at high speed and unsteady. This aspect is the biggest challenge for the injection of microbubbles and gas layers as it is impossible to maintain the bubbly-layer close to the surface in unsteady motion. In a recent review article on the lubrication of external liquid flow with bubbles or gas layers (Ceccio 2010), unsteady flows that cause the break up of air layers leading to large increases in drag were highlighted as the most significant challenge. A potentially viable drag reduction technique should be insensitive to vessel motion. As an alternative, we propose the application of passively produced plunging motion for high speed hydrofoil vessels. Within the field of unsteady aerodynamics it is well established (Jones et al. 1998; Young and Lai 2004; Tuncer and Kaya 2005; Cleaver et al. 2011; Cleaver et al. 2012) that the drag coefficient of a plunging foil is significantly less than that of a steady foil even to the extent that it is possible for the plunging foil to create thrust. Furthermore the technique is well established in nature (Barrett et al. 1999), and has previously been applied (Naito and Isshiki 2005) to low speed vessels to extract wave energy and improve stability.

Foil oscillations reduce drag through the Knoller-Betz effect. A stationary foil will shed vortices in the classic Kármán vortex street pattern. This is taken to be drag

indicative due to the momentum deficit in the wake. As the airfoil is oscillated with increasing frequency or amplitude the positions of these vortices will be gradually inverted to create a reverse-Kármán vortex street. This is taken to be thrust indicative due to the momentum surplus in the wake. The most influential parameter in determining the thrust performance of the motion is generally accepted as the nondimensional plunge velocity, $Sr_A = fA/U_\infty$. It is therefore effective for both high-frequency small-amplitude motion, and low-frequency large-amplitude motion.

For a high speed hydrofoil vessel there are two possible methods of creating the motion, either actively through forced motion (Fig. 1a) or passively through wave motion (Fig. 1b). The active scenario will give the greatest control but will also require work input. The passive scenario is the more interesting possibility as it requires no work input (Grue et al. 1988) and indeed any hydrofoil passing through waves will experience the effect regardless of whether it is intended. In essence as the craft passes through the waves it will be subject to an oscillatory freestream due to both the oscillatory flow within the waves and also the motion of the vessel reacting to the waves. The maximum possible amplitude of this motion is therefore the amplitude of the wave at the surface, and the frequency of the motion can be estimated through the wave encounter frequency, $f \approx U_\infty/\lambda_w$. Using these definitions a selection of realistic wave amplitudes and frequencies from the Pierson-Moskowitz sea spectrum (Pierson and Moskowitz 1964), are shown as symbols in Fig. 2 for two possible hydrofoil chord lengths. Conveniently this real wave data approximately collapses onto a constant Strouhal number based on amplitude of $Sr_A = 0.076$ which is independent of vessel speed, hydrofoil chord length and sea state. Although this real wave data represents a possible operating scenario it is solely for the significant wave as derived from a wave spectra, and therefore does not give a maximum Sr_A. Thus to

give an absolute upper bound, also shown is the value for a Stokes ideal wave of A/λ_w = 1/7, or alternately Sr_A = 0.142 (Michell 1893; Tsuji and Nagata 1973). This is a theoretical value for an ideal wave of maximum steepness which realistically will not be surpassed and therefore represents an excellent upper bound for the experiments.

For experimental convenience we shall model the passive scenario as an oscillatory foil in a steady freestream (the active scenario). Such a situation has been theoretically studied by Grue et al. (1988) and computationally by Zhu et al. (2006) as a method of propulsion. It was found that the thrust was generally diminished by proximity to the free surface, both directly through the energy expended in wave production, and indirectly through the effect these waves have on the pressure forces over the airfoil. This drag enhancing effect was particularly pronounced around an unsteady parameter of $\tau_c = U_\infty 2\pi f/g$ = 0.25 due to significant wave formation. The detailed study of Silva and Yamaguchi (De Silva and Yamaguchi 2012) computationally considered a hybrid of the two scenarios in Fig. 1, an actively plunging-pitching hydrofoil tuned to the incoming wave so as to actively create thrust and extract wave energy. It was shown that up to 93% of the incoming wave energy could be recovered resulting in a maximum of 18% improvement in propulsive efficiency. These results are for a single selection of parameters (depth, plunging amplitude, plunging frequency etc), greater improvements are therefore feasible.

To investigate the possibility of drag reduction through small-amplitude airfoil oscillation, this paper shall examine two aspects: the effect of amplitude and the effect of depth. The experiments consist of a NACA 0012 airfoil at an angle of attack of α = 0° plunging vertically under a free surface at plunge velocities up to Sr_A = 0.16. The motion is sinusoidal as this is the best approximation possible to the two scenarios shown in Fig. 1. To understand the effect of amplitude, force and particle image

velocimetry results will be presented for five amplitudes ($0.1 \leq a/c \leq 0.5$) at a single depth ($d/c = 2.25$), where there are no free surface effects. To understand the effect of depth this will be expanded to consider depths in the range: $d/c = 0.5$ to 2.25.

2 Experimental Apparatus and Procedures

Force and Particle Image Velocimetry (PIV) measurements were conducted on a plunging NACA 0012 airfoil mounted horizontally in a closed-loop water channel, see Fig. 3. For a review of parameters studied, see Table 1; uncertainties are calculated based on the methods of Moffat (1985) taking into account both bias and precision errors. Note that Strouhal number is directly related to the reduced frequency through: $Sr_c = k/\pi$.

Table 1 Experimental Parameters

Parameter	Range Considered	Uncertainty
Re	40,000	+/- 200
α	0°	+/- 0.5°
a/c	0.1 to 0.5	+/- 0.003
c	0.1	+/- 0.005
d/c	0.5 to 2.25	+/- 0.02
Fr	0.43	+/- 0.03
Sr_c	0 to 0.8	+/- 2.3%
Sr_A	0 to 0.16	+/- 0.0012
U_∞	0.43	+/- 0.03

2.1 Experimental Setup

The experiments were conducted in a free-surface closed-loop water channel (Eidetics Model 1520) at the University of Bath. The water channel is capable of flow speeds in the range 0 to 0.5 m/s and has a working section of dimensions 381 mm x 508 mm x 1530 mm. The turbulence intensity has previously (Heathcote 2006) been measured by laser Doppler velocimetry (LDV) to be less than 0.5%.

Mounted on top of the channel is the experimental rig, see Fig. 3b. This consists of a carriage mounted on New Way air bushings, which is driven by an Aerotech BLMC linear motor controlled by an Aerotech Soloist CP controller with position feedback from a Renishaw Signum optical encoder. This system was capable of achieving sinusoidal oscillations of arbitrary amplitude and depth with a maximum recorded position error of < 30 μm. Attached to this carriage is the binocular force balance described below. The wing is attached to the force balance through two, 2 mm thick, streamlined stainless steel stings mounted at either end. The wing spanned the test section wall to wall with a 2 mm clearance so as to minimize three-dimensional effects. The wing was constructed by selective laser sintering from glass filled polyamide.

At operating conditions the water channel had a depth of 0.45 m. The results for section 3.1 (Effect of amplitude) are for a depth of $d/c = 2.25$. This is therefore half way between the bottom of the water channel and the free surface. As will be demonstrated, at this depth the free surface has no effect. The blockage ratio is 2.7%. The closest proximity between the airfoil and tunnel walls is 1.75c in the $d/c = 2.25$, $a/c = 0.5$ case. Given that the free surface has no measurable effect on the thrust coefficient (see Fig. 4 and discussion later) in the $d/c = 2.25$ case the lower wall will likewise have negligible effect. The effect on the vortical flow field can be approximated by estimating the velocity induced by the mirror image on a TEV, using the Biot-Savart law ($U_{TEV} = \Gamma/2\pi h$), where $h/2$ is the distance to the wall. The peak circulation for $Sr_A = 0.16$ is approximately: $\Gamma/U_\infty c = 0.52$, which gives a maximum wall-induced TEV velocity of 2.4% of the freestream velocity.

2.2 Force Measurements

The force in the streamwise direction was measured through a binocular strain gauge force balance (Frampton et al. 2000). Two force balances of differing rigidities were used so as to achieve the desired accuracy whilst minimizing flexibility. The signal from the strain gauges was amplified by a Wheatstone bridge circuit and sampled at either 2 kHz for 21,600 samples (stationary cases), or 360 per cycle for 60 cycles (dynamic cases). The forces were then calculated from the average voltage through linear calibration curves. The calibration curves consisted of thirteen points, and were performed daily before testing. Each data set was repeated at least once and then averaged.

To validate the accuracy of the method, force measurements were performed for a/c = 0.1 and 0.2 and compared to those taken using the vertical rig described in Heathcote et al. (2008), Calderon et al. (2010), and Cleaver et al. (2011; 2012) with the same experimental conditions. This vertical rig is an entirely different setup which mounts the airfoil vertically between two end plates and therefore does not experience free surface effects. Despite the significant differences the agreement between the two is excellent, see Fig. 4. The drag coefficient for the stationary airfoil was measured as: C_{D0} = 0.029 for Re = 40,000.

2.3 PIV Measurements

The flow was seeded with 8 – 12 μm hollow glass spheres. The velocity field around the airfoil was measured using a TSI Inc. 2D-PIV system incorporating a dual ND:YAG 50 mJ pulsed laser, 2 MP Powerview Plus 12 bit CCD camera and TSI Model 610034 synchronizer. For the majority of the measurements the laser was

positioned behind to illuminate a mid-span streamwise plane with the camera positioned to the side as shown in Fig. 3a. For the measurements over the leading-edge region at d/c = 0.5 it was necessary to reposition the laser above the free surface, aimed downwards, so as to capture the free surface and the leading-edge region. The location of the phase-averaged free surface was extracted by averaging all of the phase-locked images to give a single image with the free surface highlighted as a high intensity region (due to laser reflections). This technique had an accuracy of +/- 3mm, primarily due to blurring of the phase-averaged free surface resultant from wandering of the instantaneous free surface. The PIV images were analyzed using the software Insight 3G. A FFT correlator using interrogation windows of 32 x 32 pixels with 50% overlap was selected to generate a vector field of 99 x 73 vectors, approximately giving a 2 mm spatial resolution. The phase-averaged data is derived from 100 to 200 pairs of images as required; the time-averaged data is derived from 500 pairs of images. Measurements over the wake region and leading-edge region were performed separately. These were then merged in MATLAB through interpolation of the wake region data onto the leading-edge region grid using the trailing-edge as the common reference point.

3 Results and Discussion

3.1 Effect of Amplitude

Shown in Fig. 5 is the drag reduction for a NACA 0012 airfoil oscillated at the central depth, d/c = 2.25, for a range of amplitudes against non-dimensional frequency in the form of Sr_c. The levels of drag reduction are significant in comparison with the drag coefficient for the airfoil (C_{D0} = 0.029). If effectively exploited the energy contained

within an unsteady free surface could therefore represent a significant efficiency saving for a hydrofoil vessel. For all cases increasing amplitude or frequency leads to increased drag reduction. For the smaller amplitudes (a/c = 0.1 and 0.2) this trend is strongly parabolic with steeper gradient for greater amplitude. For the larger amplitudes (a/c = 0.3, 0.4 and 0.5) there is still a parabolic trend with steeper gradient for greater amplitude at lower Strouhal numbers, but at higher Strouhal numbers there is a 'kink' which causes a break from this trend. We shall return to this later. The strong amplitude dependence is expected since Garrick approximations (Garrick, 1936) predict the thrust (drag reduction) from an oscillating airfoil to be:

$$C_T = \pi^3 Sr_A^2 (F^2 + G^2) \qquad (1)$$

where F and G are the Theodorsen functions which are weakly dependent on the non-dimensional frequency, Sr_c, and the far more influential parameter, Sr_A, is dependent on both amplitude and frequency. The parameter Sr_A can be considered as a non-dimensional plunge velocity. Since Sr_A is the more influential parameter, and as it is more applicable to our problem (see Fig. 2), any further results shall be presented against Strouhal number based on amplitude.

Figure 6 shows the same results as Fig. 5 except with Strouhal number based on amplitude on the x-axis. The collapse in the data reiterates the importance of Strouhal number based on amplitude. Also shown are dashed lines which represent the Garrick predictions for the same five amplitudes. These demonstrate parabolic trends with steeper gradient for greater amplitude. At low Strouhal number (Sr_A < 0.08) the experimental results follow these general trends but with reduced gradients in comparison with the Garrick predictions. The reduced gradient can be attributed to the limitations of the Garrick predictions. In particular, Garrick theory assumes incompressible, inviscid flow, with smooth flow separation from the trailing-edge

only, and no self-induced roll up of the wake. As demonstrated by other authors (Young and Lai 2004, 2007; Heathcote and Gursul 2007) Garrick approximations therefore tend to over-predict thrust generation. At $Sr_A \approx 0.08$ the aforementioned kink means that the larger amplitudes break from this general trend resulting in a crossover point at $Sr_A \approx 0.12$. Thus for the same plunge velocity before $Sr_A \approx 0.12$ larger *a/c* is preferable; after $Sr_A \approx 0.12$ smaller *a/c* becomes preferable. The collapse of data at this particular point is most likely coincidental, indeed the curve for *a/c* = 0.2 does not crossover the *a/c* = 0.1 curve until $Sr_A \approx 0.14$.

To investigate why larger amplitudes break from the parabolic Garrick trend, phase-averaged PIV measurements were performed for Sr_A = 0.04, 0.08, 0.12, and 0.16 for the smallest and largest amplitudes, see Figures 7 through 10. Figure 7 shows Sr_A = 0.04 at the top, middle (down), bottom, and middle (up) phases of the motion. For both amplitudes at this low Strouhal number Kelvin-Helmholtz instability dominates, generating a series of small alternating vortices which are shed at high frequency from the trailing-edge. It is interesting that these instabilities should appear in phase-averaged measurements because for the vortices not to be eradicated through the averaging process they must be locked in to the phase of the motion. Young and Lai (2007) performed a computational study on a NACA 0012 airfoil at α = 0° and *Re* = 20,000 which predicted that the airfoil would be subject to vortex lock-in in a similar manner to oscillating cylinders. This means that at low Strouhal numbers the natural shedding frequency dominates, at high Strouhal numbers the forcing frequency dominates, and in between there may be a harmonic region. In the harmonic region the airfoil may display vortex shedding at a higher harmonic of the forcing frequency, but close to the natural shedding frequency. Taking into account the natural shedding frequency (Huang and Lee 2000) at this Reynolds number and

using the lock-in boundaries presented in Young and Lai (2007), the frequency-amplitude combinations shown in Figs. 7 through 10 should be within the harmonic region. Hence the shedding is not random but a harmonic of the plunging frequency resultant from the interplay between the natural shedding and forcing frequency, and the vortices are therefore locked-in to the phase of the motion and visible in a phase-averaged sense. According to the predictions of Young and Lai (2007) this phenomenon will persist to higher Sr_A for larger amplitudes.

Figure 8 shows the results for $Sr_A = 0.08$, which is the point at which $a/c = 0.5$ breaks from the Garrick trend. The trailing-edge vortices are now stronger and the forcing frequency is becoming more dominant. This is more clearly exhibited for $a/c = 0.1$ where multiple vortices are being shed per half cycle but they are being shed in groups locked into the phase of the motion. Hence during the downward motion multiple counter-clockwise vortices emanating from the lower surface shear layer are shed, and during the upward motion multiple clockwise vortices emanating from the upper surface shear layer are shed. As the vortices are being shed in groups locked in to the motion it is now possible to approximately measure the trailing-edge vortex (TEV) shedding frequency to demonstrate how it relates to the natural shedding frequency. The TEV shedding frequency can be approximately measured by counting the number of TEV shed per cycle and dividing by the period T. For $a/c = 0.1$, depending on the phase selected (see Fig. 8 left), the number of TEV shed per cycle lies in the range eight to ten. Given the Strouhal number of $Sr_c = 0.4$ this gives a natural frequency of $Sr_c = 3.2$ to 4 which is in very good agreement with the computationally measured natural shedding frequency of $Sr_c = 3.0$ (Young and Lai 2007) for $Re = 20{,}000$ and experimentally measured values of $Sr_c = 2.7$ (Koochesfahani 1989) for $Re = 12{,}000$, and $Sr_c = 4.3$ (Huang and Lee 2000) for $Re =$

40,000. Note that the natural shedding frequency is Reynolds number dependent in this regime due to the presence of Reynolds dependent separation; see Huang and Lee (2000) and Huang and Lin (1995) for more detail.

Likewise the TEV shedding frequency can be approximated for Sr_A = 0.12 (Fig. 9), in this case there are six TEVs shed per cycle which equates to a frequency of Sr_c = 3.6 in good agreement with the natural shedding frequencies given above. Note that Sr_A = 0.12 is after the a/c = 0.5 drag reduction curve breaks from the theoretical Garrick trend. There is now significantly different behavior for a/c = 0.5. At the top of the motion there is a large counter-clockwise leading-edge vortex below the trailing-edge; likewise at the bottom of the motion there is a large clockwise leading-edge vortex (LEV) above the trailing-edge. These convected LEVs are unstable and lose their coherency more rapidly as evidenced by their rapid dissipation in a phase-averaged sense. Similar unstable LEVs have been shown to exist at lower Reynolds numbers for smaller amplitudes and higher frequencies (Cleaver et al. 2011) and the instability has been shown to be promoted by higher Reynolds numbers (Visbal 2009). In these cases, spanwise instabilities resulted in their abrupt breakdown and complete dissipation. In the current measurements the convected LEV is weak but still existent. Garrick approximations assume no separation; the presence of leading-edge vortices at larger amplitudes is therefore a strong explanation for the break from the Garrick trends. The presence of stronger, larger LEVs at larger amplitudes has also been documented by Baik *et al.* (2012) (compare cases N1, N5 and N6), and McGowan *et al.* (2011) (compare cases 1A, 3A and 4A). The effect of these LEVs on thrust coefficient is however often contradictory. Tuncer *et al.* (1998) demonstrated deteriorating thrust performance due to leading-edge separation for a plunging NACA 0012 airfoil. The onset of separation was found to be $Sr_A \approx 0.11$, but this became a

poor approximation at smaller amplitudes (a/c < 0.3) where larger plunge velocities were required. Similarly Young and Lai (2007) concluded that leading-edge separation reduces propulsive efficiency for pure-plunge and pitch-plunge cases in comparison with Garrick approximations and panel codes which both assume no separation. For the pure-plunge case the LEV was found to form a low pressure region over the airfoil, but the negative pressure coefficients associated with this LEV were significantly lower than those predicted by an inviscid panel method which assumes no separation and therefore represents a theoretical 'no-separation' case. The very presence of the LEV therefore reduces thrust compared to inviscid theory, which is also supported by the results of Pan *et al.* (2012). In contrast Anderson *et al.* (1998) showed that leading edge separation was associated with higher thrust. In particular the comparison of their cases V-2, VI-2 and III-2 showed increased thrust with increased circulation of the leading-edge vortex. However, the motion used in Anderson *et al.* (1998) was a combined pitch-plunge motion and their own results show that phase between pitch and plunge is crucial. This shows that the presence of LEVs may be detrimental or beneficial to thrust creation depending on the motion of the airfoil.

The question is therefore why are smaller amplitudes less prone to separation and LEVs despite having the same maximum plunge velocity and therefore the same peak effective angle of attack? The core reason for this difference is that to achieve the same Sr_A at larger amplitude requires lower frequency, thus there is a larger formation and convection time per cycle. A similar conclusion was reached by Young and Lai (2007). It is therefore necessary to also consider Sr_c, as this represents a ratio of the convection time scale (c/U_∞) to the motion time scale (f).

Figure 10 show the results for Sr_A = 0.16, which is now after the crossover point. For *a/c* = 0.1 the vortices are now much stronger and the forcing frequency is clearly dominant although there are still multiple TEVs shed per half cycle suggesting that it is still within the harmonic region. These TEVs form a clear reverse-Kármán vortex street. There is a small LEV very close to the lower surface of the airfoil at the top of motion which convects along the lower surface gradually dissipating. For *a/c* = 0.5 the convected LEVs are now much stronger and dominate the flow field, see top and bottom of the motion.

In summary, the difference between the two amplitudes at higher Sr_A is that *a/c* = 0.1 is characterized by shedding of vorticity from the trailing-edge leading to a clear reverse-Kármán vortex street; whereas *a/c* = 0.5 is characterized by shedding from the leading-edge and diminished thrust performance. For *a/c* = 0.1 vortex lock in is apparent across the entire Strouhal number range; whereas for *a/c* = 0.5 vortex lock-in is only apparent whilst shedding continues from the trailing-edge.

3.2 Effect of Depth

Shown in Fig. 11 are drag reduction measurements for four further depths: *d/c* = 2.00, 1.50, 1.00 and 0.50, and all five amplitudes. As one would expect *d/c* = 2.00 (Fig. 11a) is so close to the central depth (*d/c* = 2.25, Fig. 6) that the curves are essentially the same for all amplitudes. The only noticeable difference is perhaps the presence of a very weak peak at Sr_A = 0.09 for *a/c* = 0.2 (note the change in gradient); however this is contained within the bounds of experimental uncertainty and therefore cannot be confirmed as real.

At *d/c* = 1.50 (Fig. 11b) the peak at Sr_A = 0.09 for *a/c* = 0.2 is now clear and distinct. There are also further peaks for *a/c* = 0.3 at Sr_A = 0.13 and *a/c* = 0.4 at $Sr_A \approx$

0.16, although this last peak could actually be outside the measured range. Except for the existence of these peaks the general Garrick trends still hold true at low Strouhal numbers. At high Strouhal numbers the data has become more disordered and there is no longer a clear crossover point.

At d/c = 1.00 (Fig. 11c) the Garrick trends at low Strouhal number are now beginning to break down and there is a general departure from the behavior observed for the central depth. Furthermore the peaks are now very distinct and occur at the same Strouhal numbers as for d/c = 1.50 with only minor deviation. In addition there is potentially a fourth weak peak for a/c = 0.1 at $Sr_A \approx 0.05$.

At d/c = 0.50 (Fig. 11d) the peak for a/c = 0.1 is now clear at Sr_A = 0.04 and the peaks for the other amplitudes are further accentuated. There is no longer any of the trends that were observed for the central depth. The effect of depth is therefore twofold: firstly with decreasing depth there is a gradual departure from the Garrick trends and crossover point observed for the central depth descending into more disorderly behavior; secondly drag enhancing peaks are observed at larger Strouhal numbers for larger amplitude. In addition it can also be concluded that the free surface has negligible effect on thrust coefficient at depths greater than two chord lengths. This is in agreement with the earlier comparison shown in Fig. 4 and the computational results of Zhu et al. (2006) for a horizontal NACA 0012 wing oscillating under a free surface.

Zhu et al. (2006) also observed similar drag enhancing peaks. They attributed the cause to be oscillation at or around a critical unsteady parameter of $\tau_c = U_\infty 2\pi f/g$ = 0.25. This critical parameter was theoretically predicted by Grue and Palm (1985) and Palm and Grue (1999). To demonstrate this effect shown in Fig. 12 are the same

results as Fig. 11 except against the unsteady parameter, τ. The peaks collapse reasonably well around $\tau = 0.25$ in support of this hypothesis.

To obtain detail on the cause of the peaks, phase-averaged PIV measurements were performed for $a/c = 0.2$ and $Sr_c = 0.150$, 0.225, and 0.300, at both the central depth and the shallowest depth. The associated force measurements are shown in Fig. 13. Corresponding vorticity and velocity fields are shown in Figs. 14 through 19. The left column shows the shallowest depth, $d/c = 0.5$; the right column shows the central depth, $d/c = 2.25$. Both columns show phase-averaged measurements for the top, middle (down), bottom, and middle (up) phases of the motion.

Shown in Fig. 14 are phase-averaged vorticity measurements for $Sr_c = 0.150$, before the peak in drag coefficient, covering both the wake and the upper surface leading-edge region. The sting obscured part of the upper surface; this can be seen as the white region above $x/c \approx 0.7$. For $d/c = 0.5$ the free surface is demarked by a solid black line. At the top of the motion (Fig. 14a left) the free surface is characterized by small-amplitude long-wavelength undulations. As the airfoil moves down (Fig. 14b left) the free surface deforms to produce a steep wave above the trailing-edge of the airfoil. Under the surface there is a small region of counter-clockwise vorticity. Similar regions of counter-clockwise vorticity have been observed below steady or quasi-steady spilling breaker waves, see Lin and Rockwell (1995), Dabiri and Gharib (1997), and Belden and Techet (2011). At the bottom of the motion (Fig. 14c left) this steep wave collapses creating a large region of counter-clockwise vorticity emanating from the free surface minimum above $x/c \approx 0.5$. This vorticity is more characteristic of the mixing layer created by sharp free-surface curvature, as described by Lin and Rockwell (1995). With time this vorticity convects downstream, see Fig. 14d left, and new vorticity ceases to be created at the surface. In general, the unsteady wave and

vorticity formation due to an oscillating airfoil is more complicated than the steady wave formation studied in the literature. Comparing the flow field for the central depth with that for d/c = 0.5, there are minor differences in terms of strength of the trailing-edge shear layer (Fig. 14b) and shear layer instabilities (Fig. 14 a and c), but generally the flow fields are very similar reflecting the similar level of drag reduction.

Shown in Fig. 15 are the measurements for Sr_c = 0.225, i.e., at the peak in drag coefficient. For this Strouhal number the trailing-edge vortices are stronger and the wave formation is much more pronounced. At the bottom of the motion (Fig. 15c) there is a steep wave above the trailing-edge with a region of counter-clockwise vorticity near the surface. In the next phase this wave has moved upstream (above *x/c* ≈ 0.75) and the vorticity is now more characteristic of a mixing layer. This wave continues to move upstream (above the leading-edge in Fig. 15a, and upstream of the left hand side of the measurement volume in Fig. 15b). Now comparing the measurements for the central depth with those for d/c = 0.5, there are again minor differences. Of particular interest is the apparent acceleration of the clockwise TEV (note its relative downstream position in Fig. 15a). This is a result of its interaction with the shed counter-clockwise free-surface vorticity (similar to a dipole). Likewise the counter-clockwise TEV appears to be decelerated (note its relatively upstream position in Fig. 15c). A similar reduction in convection velocity for a shed counter-clockwise vortex in close proximity to the free surface was observed by Reichl et al. (2005) for the von Kármán vortex street behind a stationary cylinder. Despite these minor differences there is nothing substantial enough to explain the larger drag coefficient for *d/c* = 0.5. One can only conclude that although significant wave formation is evident, as would be expected at this value of unsteady parameter, these waves affect the airfoil through irrotational effects, this will be demonstrated later.

Shown in Fig. 16 are the measurements for Sr_c = 0.300, i.e., after the peak in drag coefficient. The trailing-edge vortices are now stronger and shed in groups locked into the phase of the motion and the wave formation is significantly diminished resulting in several smaller waves. Due to the smaller wave formation the free-surface vorticity is comparatively less and the effect of this vorticity on the convective velocity of the clockwise trailing-edge vortex is also diminished (see Fig. 16a). Nevertheless, the counter-clockwise TEV is still decelerated through interaction with the free surface (see Fig. 16d). Again despite these minor differences between the two depths the flow fields are generally similar justifying the similar levels of drag reduction shown in Fig. 13.

Shown in Figures 17 to 19 are contour plots of the magnitude of the velocity vector with streamlines superimposed. In some cases the streamlines end or start on the airfoil or the free surface. This is due to both the airfoil and free surface being in motion. Sr_c = 0.150 (Fig. 17) is before the d/c = 0.50 peak. As previously discussed, for this Strouhal number there is some minor wave formation, most prominently in the middle (down) phase (Fig. 17b). Despite this wave formation the flow fields for the two depths are relatively similar. There is a region of lower velocity over the leading-edge at the top of the motion (Fig. 17a left), and a slightly high velocity region over the aft of the airfoil in the middle (down, Fig. 17b left) and bottom phases (Fig. 17c left).

Figure 18 shows the velocity field for Sr_c = 0.225, which is at the drag coefficient peak for d/c = 0.50. As previously observed, the wave formation is significantly larger for this Strouhal number. This is consistent with the numerical simulations of Zhu et al. (2006) in that the free surface is dominated by the unsteady waves near the critical parameter. For example at the shallowest point in the motion

(Fig. 18a left) the entire leading-edge region is engulfed in a low velocity region. Note that this region is free of vorticity (see Fig. 15a left). In the next phase (Fig. 18b left) this low velocity region has propagated upstream. In addition there is a small LEV at the central depth which is absent for the shallower depth and the shape of the streamlines differ significantly. For d/c = 2.25 the streamlines curve around the LEV, whereas for d/c = 0.5 due to the motion of the free surface the streamlines generally curve towards the airfoil. At the bottom of the motion (Fig. 18c) although the streamlines are again similar for both depths, the aft of the airfoil at d/c = 0.50 is surrounded by a high velocity region, which is also free of vorticity and therefore irrotational. This is due to the strong wave formation accelerating the flow over the upper surface. A similar phenomenon was previously observed by Reichl et al. (2005) for a stationary cylinder near a free surface, and was associated with lift. In the middle phase (up, Fig. 18d) the flow fields for the first time are very similar. However, the differences between the shallow and deep cases are significant in the rest of the cycle. One would expect the combination of low velocity leading-edge region, high velocity aft region and absent leading-edge vortex to lead to a comparatively higher drag coefficient in support of the force measurements.

Figure 19 shows the velocity field for Sr_c = 0.300, which is after the drag peak for d/c = 0.50. For this Strouhal number although there is still wave formation it is significantly less, and therefore has a reduced effect on the flow field. At the top of the motion (Fig. 19a) the streamlines are similar across the two depths, although the flow is marginally decelerated by the proximity of the free surface it is much less than observed in Fig. 18a. At the middle (down, Fig. 19b) phase of the motion a LEV is apparent for both depths, although the size and position is slightly different. Proximity to the free surface inhibits LEV formation, compare phases b and c in Figures 16 and

19. The remnants of this LEV can also be seen at the central depth at the bottom of the motion (Fig. 19c). This is absent for the shallowest depth, instead the aft of the airfoil is surrounded by a high velocity region. At the next phase (Fig. 19d) the two depths are so similar as to be nearly identical. In comparison with the significant differences observed in Fig. 18 these two sets of flow fields are very similar.

In summary, the waves affect the forces over the airfoil through irrotational effects. Generally the flow is decelerated over the leading-edge region and accelerated over the aft region leading to a higher drag scenario. This effect was most pronounced at $Sr_c = 0.225$ justifying the higher drag coefficient. It can therefore be concluded that the cause of the peaks is the unsteady wave formation due to the oscillation at or near an unsteady parameter value of $\tau = 0.25$.

4 Conclusions

Experiments were performed to investigate the effect of amplitude and depth on the drag reduction resultant from plunging a NACA 0012 airfoil at an angle of attack of 0° and Reynolds number of 40,000, across a range of frequencies. The levels of drag reduction recorded could be significant for hydrofoil vessels operating under an unsteady free surface. This represents a viable option for unsteady hydrofoil vessel motion where other drag reduction techniques such as injection of bubbles and gas layers would be problematic.

Away from the free surface, at low values of Strouhal number based on amplitude, the drag reduction was shown to follow parabolic trends with steeper gradient for greater amplitude in a similar manner to the Garrick approximations. At $Sr_A \approx 0.08$ the larger amplitudes break from this trend resulting in a crossover point at $Sr_A \approx 0.12$ after

which smaller amplitudes become preferable. The cause was shown to be earlier formation of thrust inhibiting leading edge vortices at larger amplitudes. In addition, vortex lock-in phenomenon was observed for the first time experimentally. Small-scale vortices were shed from the trailing-edge at the harmonics of the plunging frequency and were therefore observed in the phase-averaged flow field.

Proximity to the surface led to a decrease in drag reduction and a general departure from these trends. In addition drag enhancing peaks were observed for the four smaller amplitudes. These were shown to depend on a critical unsteady parameter of τ_c = 0.25. At this value of τ, large scale free surface waves form that through irrotational effects significantly change the flow field in the vicinity of the airfoil inhibiting thrust creation. For depths greater than two chords the free surface has a negligible effect.

Acknowledgments

The authors would like to acknowledge the support from the Department of the Navy Grant N62909-10-1-7117 issued by the Office of Naval Research Global.

References

Barrett DS, Triantafyllou MS, Yue DKP, Grosenbaugh MA, Wolfgang MJ (1999) Drag reduction in fish-like locomotion. J Fluid Mech 392;183-212

Belden J, Techet AH (2011) Simultaneous quantitative flow measurement using PIV on both sides of the air-water interface for breaking waves. Exp Fluids 50:149-161 doi: 10.1007/s00348-010-0901-5

Calderon DE, Wang Z, Gursul I (2010) Lift enhancement of a rectangular wing undergoing a small amplitude plunging motion, AIAA 2010-386. 48th AIAA Aerospace Sciences Meeting Including the New Horizons Forum and Aerospace Exposition, Orlando, Florida

Ceccio SL (2010) Friction drag reduction of external flows with bubble and gas injection. Annual Review of Fluid Mechanics 42:183-203

Cleaver DJ, Wang Z, Gursul I (2011) Lift enhancement by means of small amplitude airfoil oscillations at low Reynolds numbers. AIAA J 49:2018 - 2033

Cleaver DJ, Wang Z, Gursul I (2012) Bifurcating flows of plunging airfoils at high Strouhal numbers. J Fluid Mech in press

Dabiri D, Gharib M (1997) Experimental investigation of the vorticity generation within a spilling water wave. J Fluid Mech 330:113-139 doi: 10.1017/s0022112096003692

De Silva L, Yamaguchi H (2012) Numerical study on active wave devouring propulsion. J Mar Sci Technol:1-15 doi: 10.1007/s00773-012-0169-y

Frampton KD, Goldfarb M, Monopoli D, Cveticanin D (2000) Passive aeroelastic tailoring for optimal flapping wings, Proceedings of Conference on Fixed, Flapping and Rotary Wing Vehicles at Very Low Reynolds Numbers, 5-7 June 2000, Notre Dame, USA

Garrick IE (1936) Propulsion of a Flapping and Oscillating Airfoil NASA Technical Report. NASA.

Grue J, Mo A, Palm E (1988) Propulsion of a foil moving in water-waves. J Fluid Mech 186:393-417 doi: 10.1017/s0022112088000205

Grue J, Palm E (1985) Wave radiation and wave diffraction from a submerged body in a uniform current. J Fluid Mech 151:257-278

Heathcote S (2006) Flexible flapping airfoil propulsion at low Reynolds numbers. Phd Dissertation, University of Bath.

Heathcote S, Gursul I (2007) Flexible flapping airfoil propulsion at low Reynolds numbers. AIAA J 45:1066-1079

Heathcote S, Wang Z, Gursul I (2008) Effect of spanwise flexibility on flapping wing propulsion. Journal of Fluids and Structures 24:183-199 doi: 10.1016/jjfluidstructs.2007.08.003

Huang RF, Lee HW (2000) Turbulence effect on frequency characteristics of unsteady motions in wake of wing. AIAA J 38:87-94

Huang RF, Lin CL (1995) Vortex shedding and shear-layer instability of wing at low-Reynolds numbers. AIAA J 33:1398-1403

Jones KD, Dohring CM, Platzer MF (1998) Experimental and computational investigation of the Knoller-Betz effect. AIAA J 36:1240-1246

Koochesfahani MM (1989) Vortical patterns in the wake of an oscillating airfoil. AIAA J 27:1200-1205

Lin JC, Rockwell D (1995) Evolution of a quasi-steady breaking wave. J Fluid Mech 302:29-44 doi: 10.1017/s0022112095003995

McCormic ME, Bhattach R (1973) Drag reduction of a submersible hull by electrolysis. Nav Eng J 85:11-16

Michell JH (1893) The highest waves in water. Philosophical Magazine Series 5 36:430-437

Moffat RJ (1985) Using uncertainty analysis in the planning of an experiment. J of Fluids Eng - Trans of the ASME 107:173-178

Naito S, Isshiki H (2005) Effect of bow wings on ship propulsion and motions. Applied Mechanics Reviews 58:253-268

Palm E, Grue J (1999) On the wave field due to a moving body performing oscillations in the vicinity of the critical frequency. J Eng Math 35:219-232

Pierson WJ, Moskowitz L (1964) A proposed spectral form for fully developed wind seas based on the similarity theory of S.A. Kitaigorodskii. J Geophys Res 69:5181-5190.

Reichl P, Hourigan K, Thompson MC (2005) Flow past a cylinder close to a free surface. J Fluid Mech 533:269-296 doi: 10.1017/s0022112005004209

Shen XC, Ceccio SL, Perlin M (2006) Influence of bubble size on micro-bubble drag reduction. Exp Fluids 41:415-424 doi: 10.1007/s00348-006-0169-y

Tsuji Y, Nagata Y (1973) Stokes' expansion of internal deep water waves to the fifth order. Journal of Oceanography 29:61-69 doi: 10.1007/bf02109505

Tuncer IH, Kaya M (2005) Optimization of flapping airfoils for maximum thrust and propulsive efficiency. AIAA J 43:2329-2336

Tuncer IH, Walz R, Platzer MF (1998) A Computational study on the dynamic stall of a flapping airfoil, AIAA Paper 98-2519. 16th AIAA Applied Aerodynamics Conference, June 15-18, 1998, Albuquerque

Visbal MR (2009) High-fidelity simulation of transitional flows past a plunging airfoil. AIAA J 47:2685-2697 doi: 10.2514/1.43038

Winkel ES, Oweis GF, Vanapalli SA, Dowling DR, Perlin M, Solomon MJ, Ceccio SL (2009) High-Reynolds-number turbulent boundary layer friction drag reduction from wall-injected polymer solutions. J Fluid Mech 621:259-288 doi: 10.1017/s0022112008004874

Young J, Lai JCS (2004) Oscillation frequency and amplitude effects on the wake of a plunging airfoil. AIAA J 42:2042-2052

Young J, Lai JCS (2007) Vortex lock-in phenomenon in the wake of a plunging airfoil. AIAA J 45:485-490 doi: 10.2514/1.23594

Zhu Q, Liu Y, Yue D (2006) Dynamics of a three-dimensional oscillating foil near the free surface. AIAA J 44:2997-3009

Figures

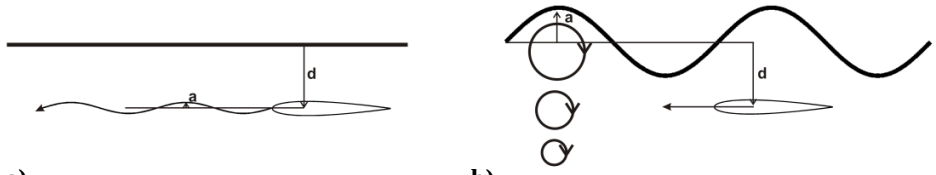

Fig. 1 Scenarios for hydrofoil unsteadiness: **a** forced motion in calm water, and **b** passive motion due to wave unsteadiness.

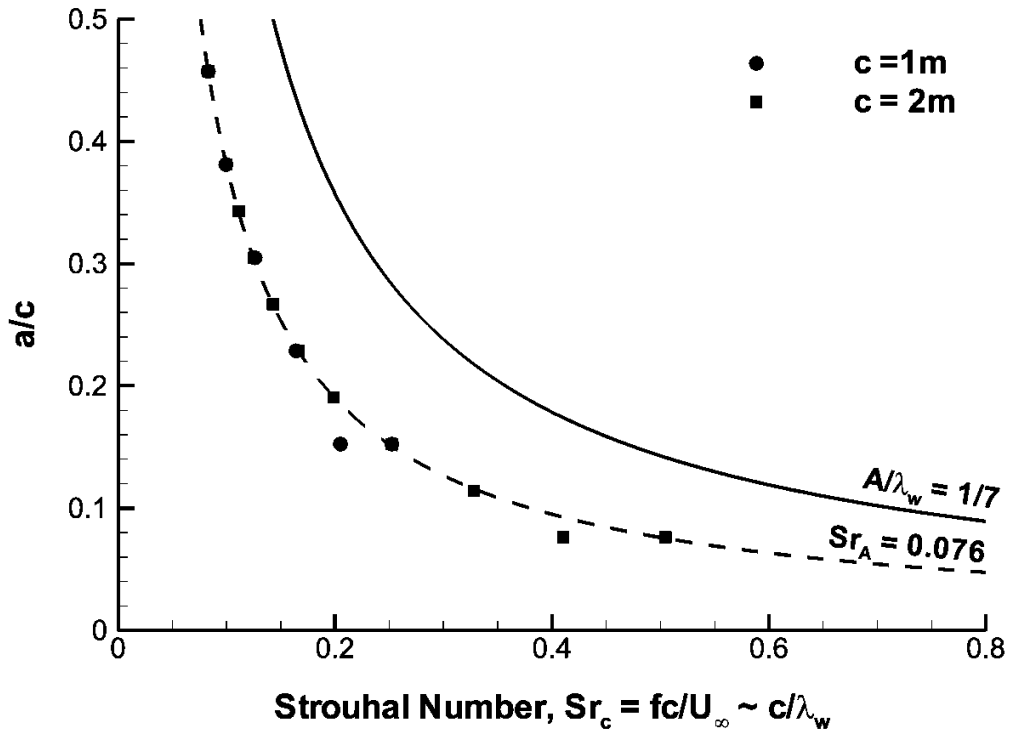

Fig. 2 Range of experimental parameters. Symbols represent values from sea state tables assuming a chord length of c = 1 m or 2 m, dashed line represents constant Sr_A = 0.076, and solid line represents constant A/λ_w = 1/7 (Sr_A = 0.142) as predicted for a Stokes ideal wave.

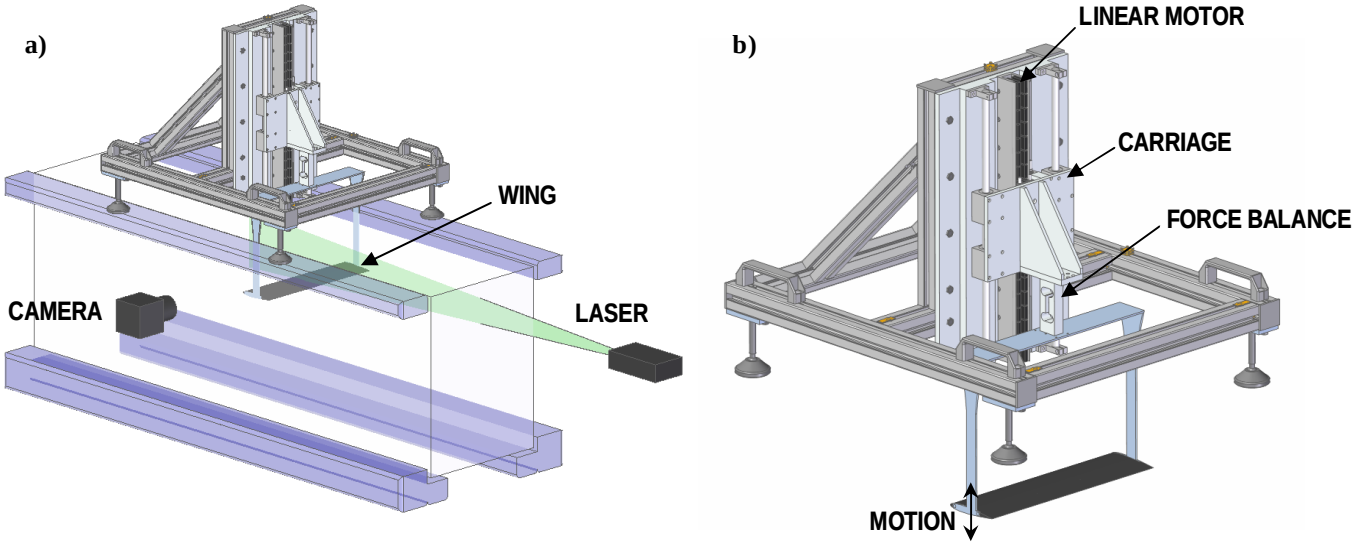

Fig. 3 a Test section with PIV equipment, and **b** experimental rig.

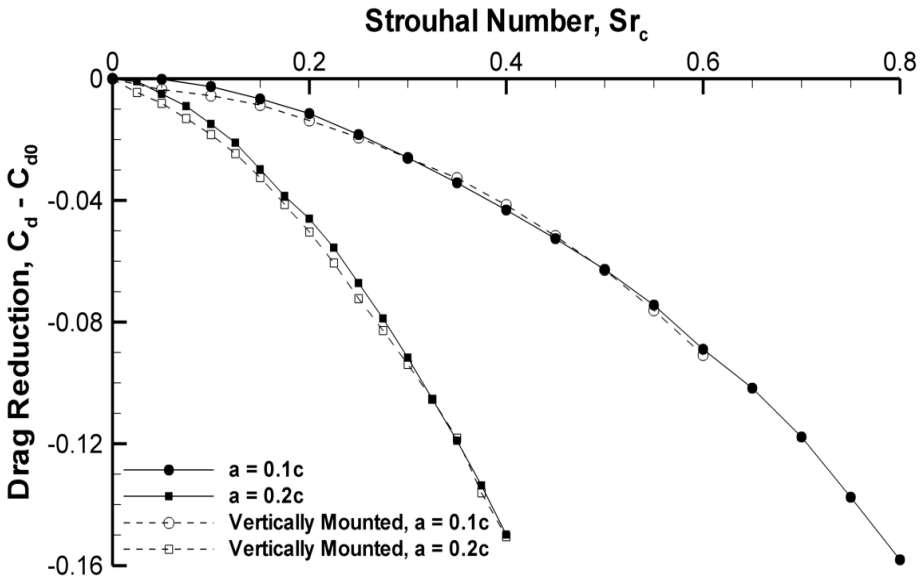

Fig. 4 Comparison of results obtained with the current experimental setup and the vertical rig as previously used in Heathcote et al. (2008), Calderon et al. (2010), and Cleaver et al. (2011; 2012).

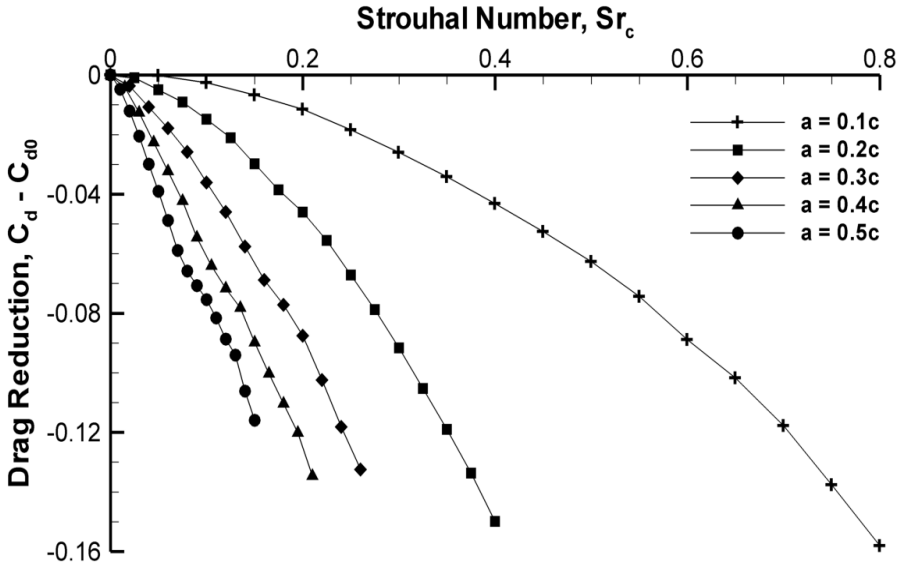

Fig. 5 Reduction in time-averaged drag coefficient against Strouhal number based on chord length for a NACA 0012 airfoil oscillated at the central depth (*d/c* = 2.25).

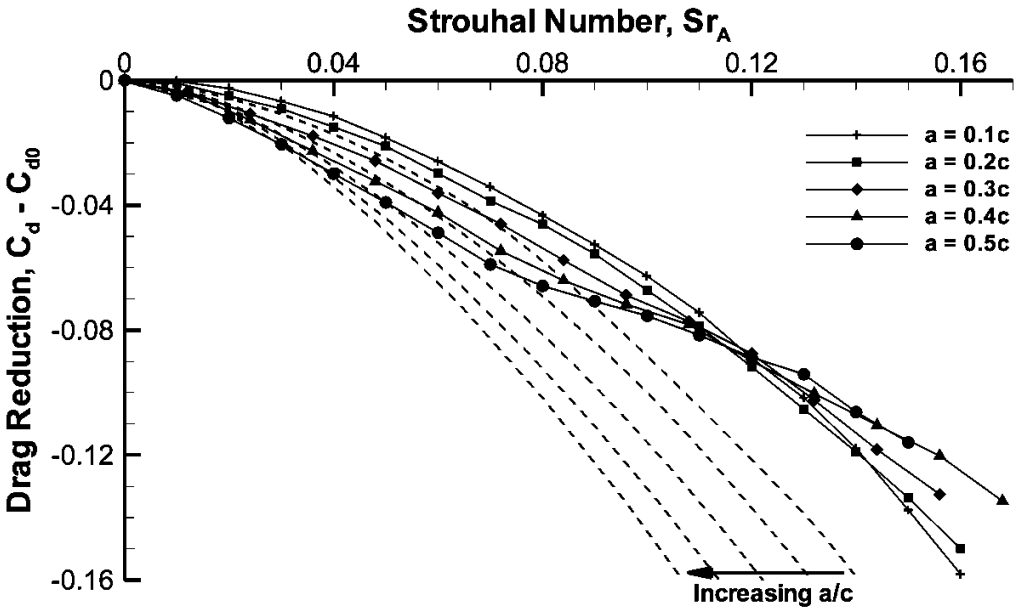

Fig. 6 Reduction in time-averaged drag coefficient against Strouhal number based on amplitude for the central depth (*d/c* = 2.25). Dashed lines represent Garrick approximations for the same amplitudes.

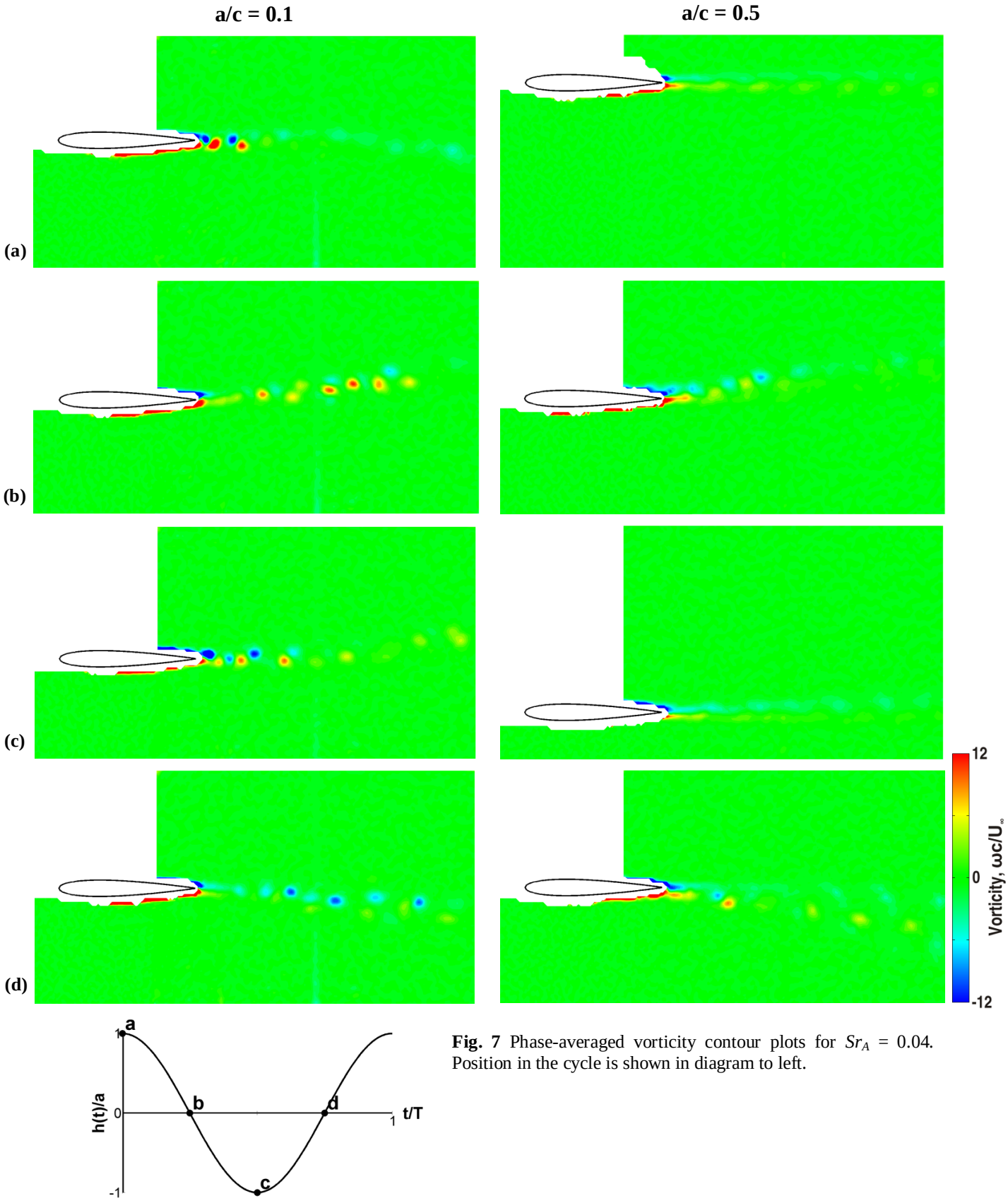

Fig. 7 Phase-averaged vorticity contour plots for Sr_A = 0.04. Position in the cycle is shown in diagram to left.

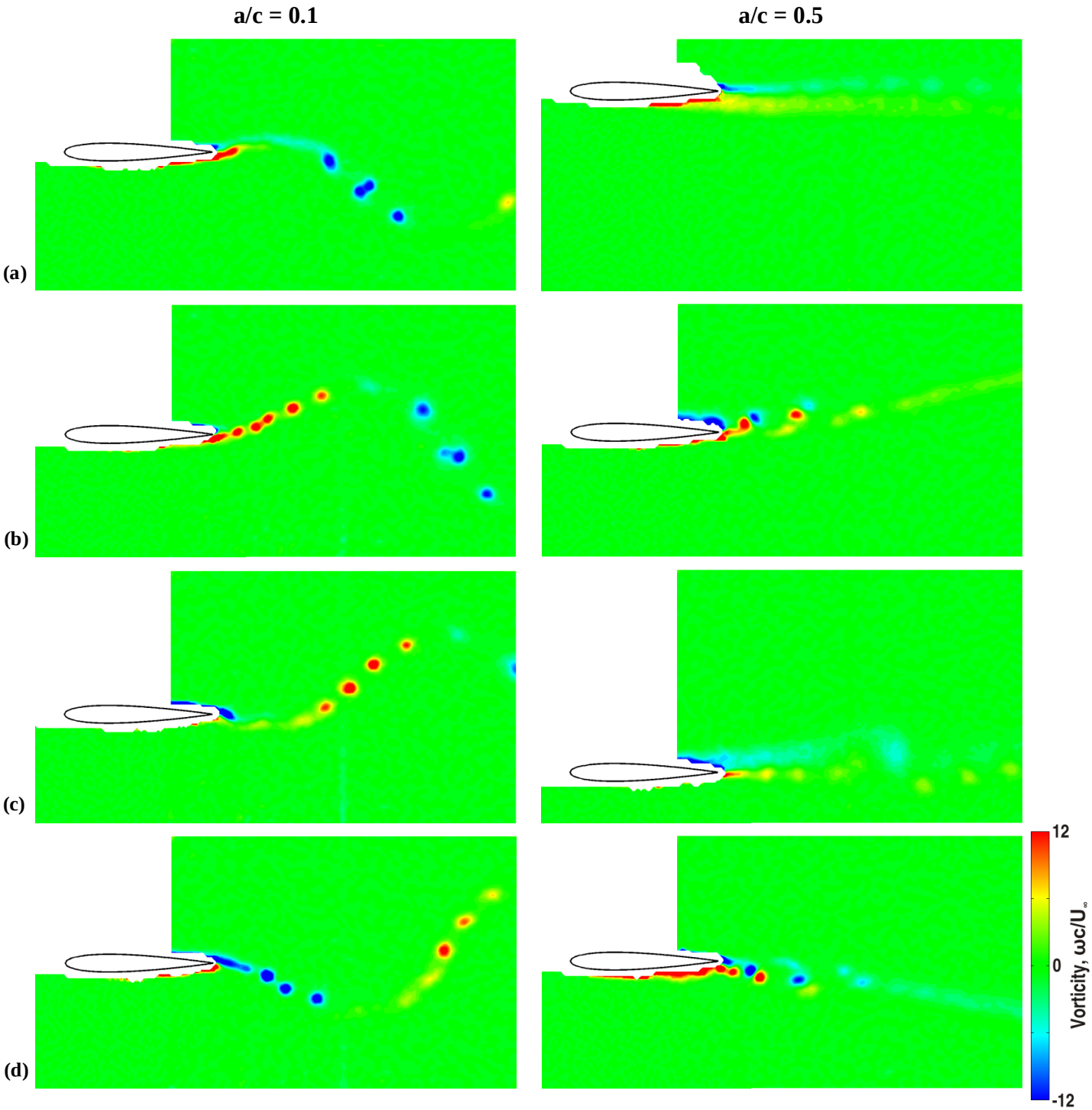

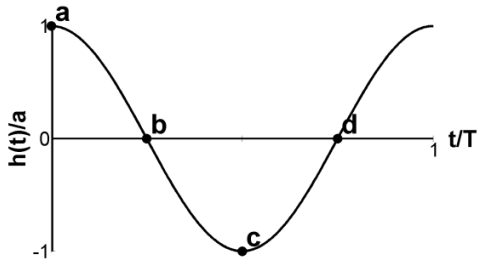

Fig. 8 Phase-averaged vorticity contour plots for Sr_A = 0.08. Position in the cycle is shown in diagram to left.

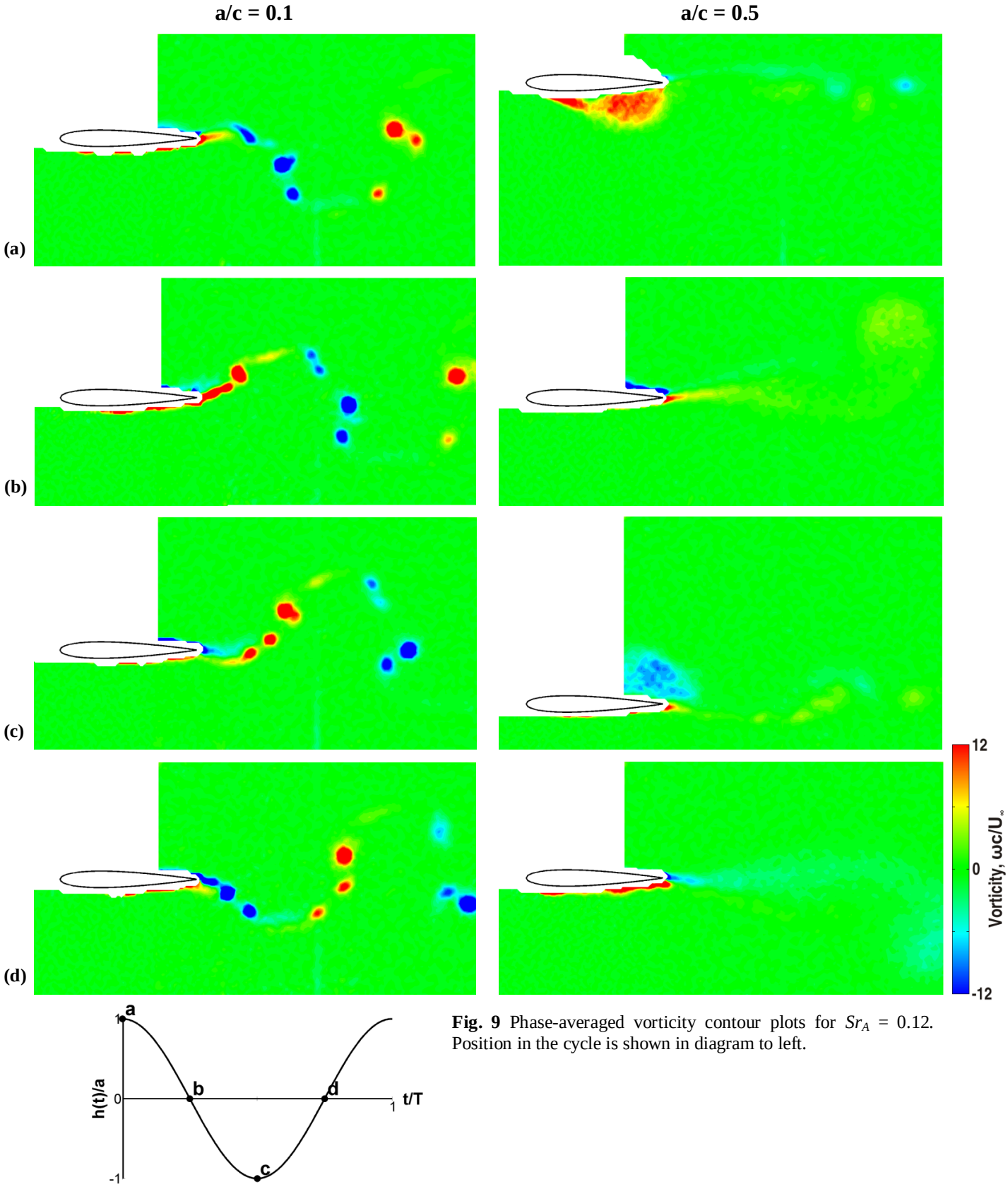

Fig. 9 Phase-averaged vorticity contour plots for Sr_A = 0.12. Position in the cycle is shown in diagram to left.

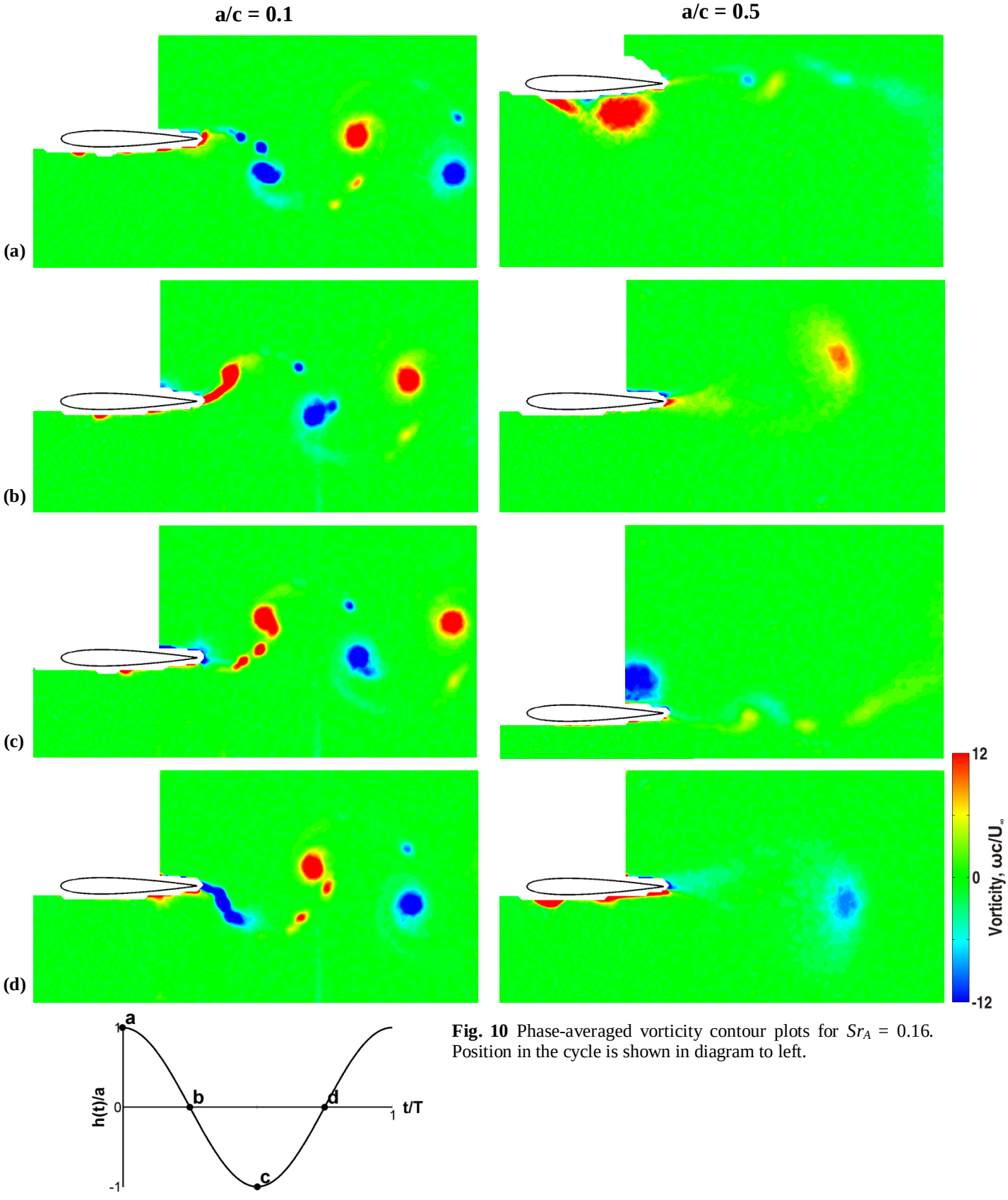

Fig. 10 Phase-averaged vorticity contour plots for Sr_A = 0.16. Position in the cycle is shown in diagram to left.

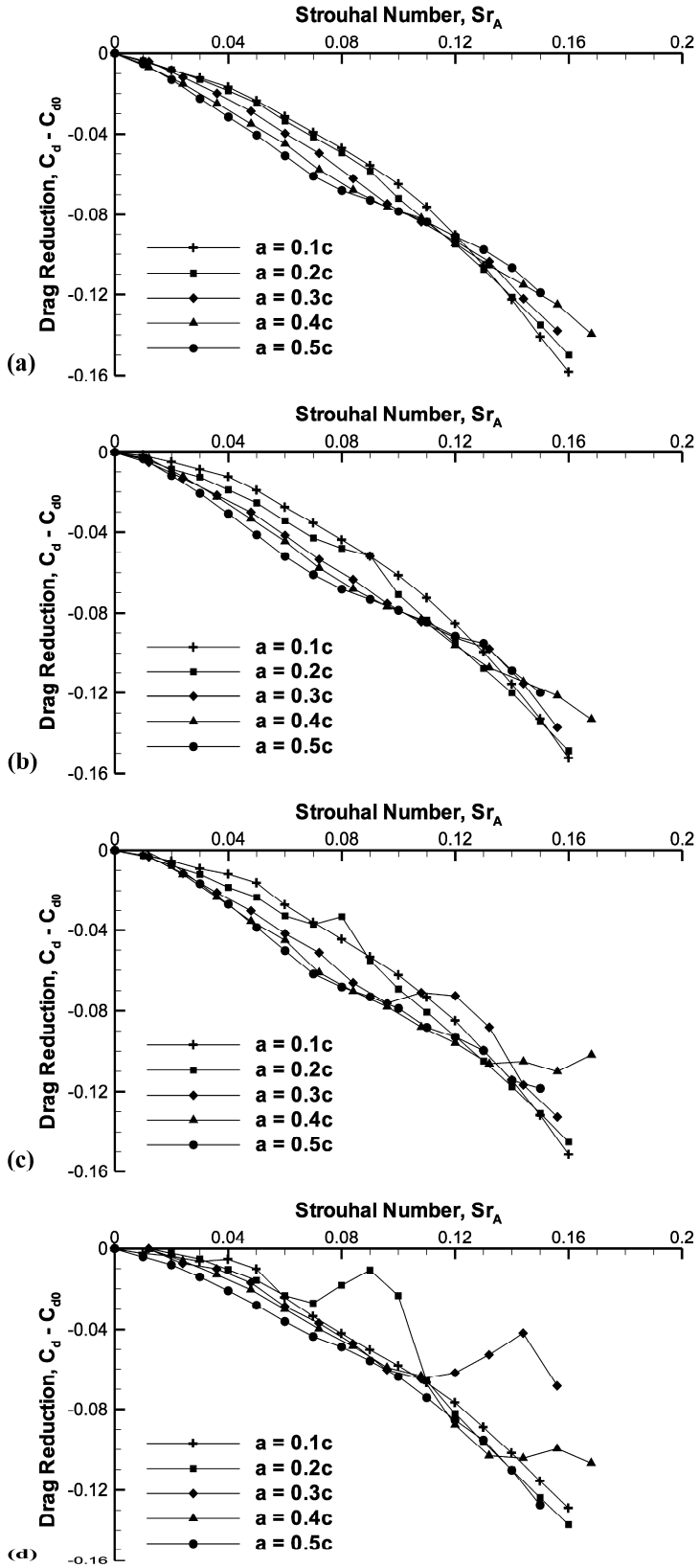

Fig. 11 Reduction in time-averaged drag coefficient against Strouhal number based on amplitude for depths of: **a** *d/c* = 2.0, **b** *d/c* = 1.5, **c** *d/c* = 1.0, and **d** *d/c* = 0.5.

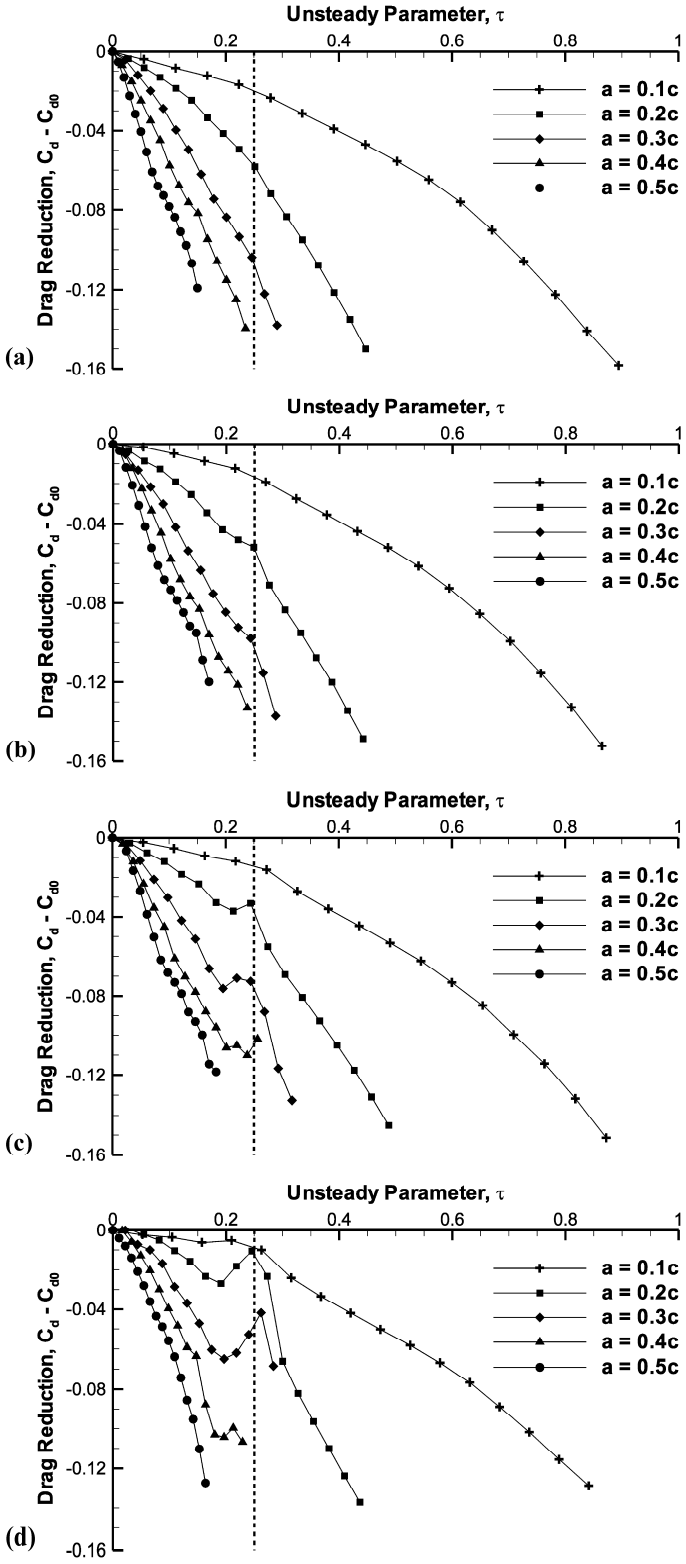

Fig. 12 Time-averaged reduction in drag coefficient against unsteady parameter for depths of: **a** *d/c* = 2.0, **b** *d/c* = 1.5, **c** *d/c* = 1.0, and **d** *d/c* = 0.5.

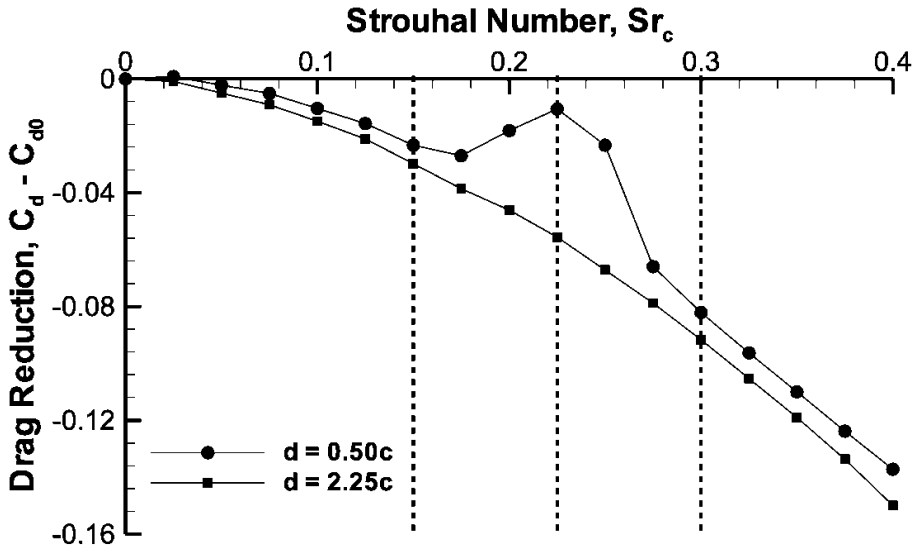

Fig. 13 Reduction in time-averaged drag coefficient against Strouhal number based on chord length for *a/c* = 0.2. Dashed lines denote the Strouhal numbers used in Figs. 14 through 19.

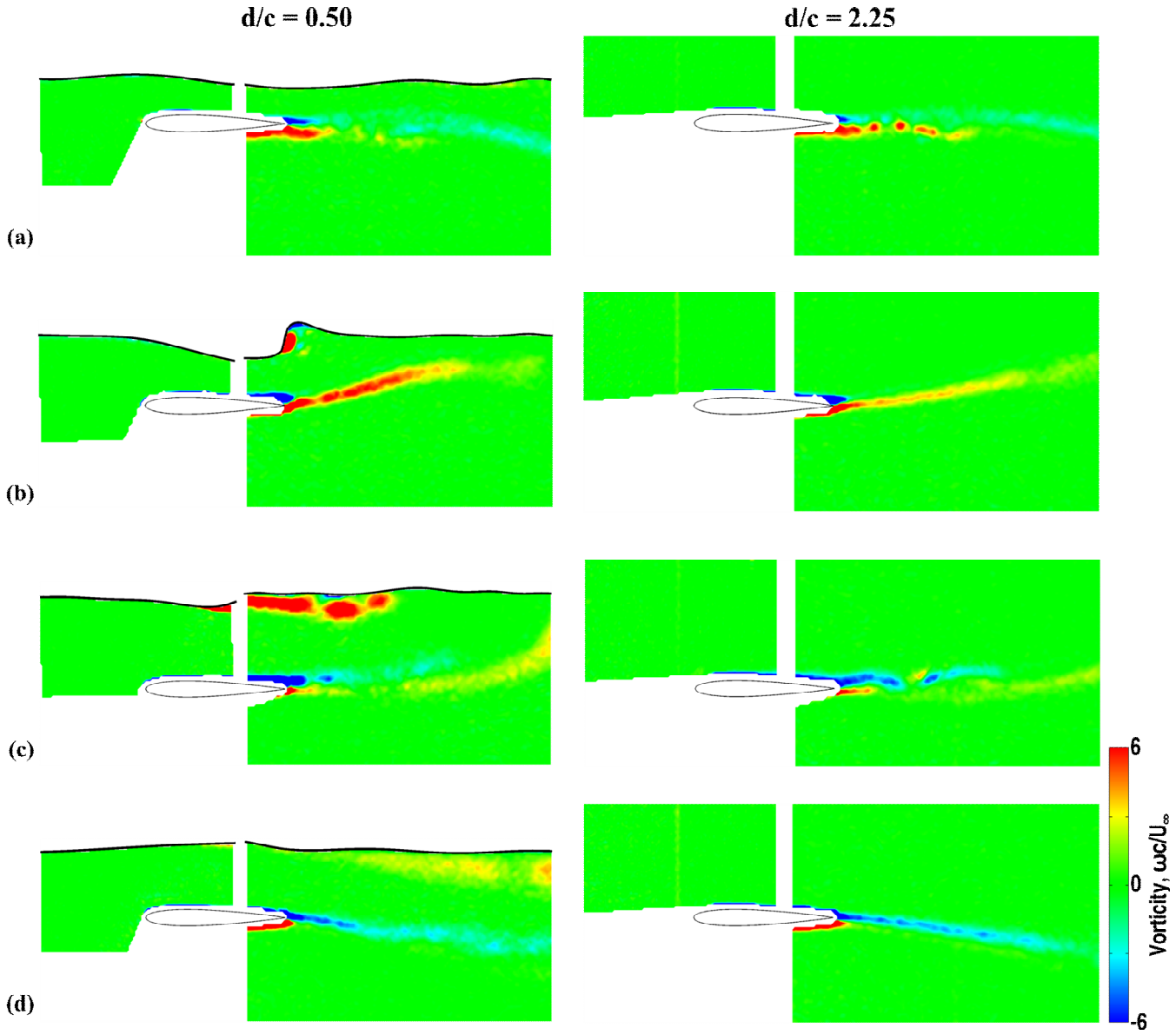

Fig. 14 Phase-averaged vorticity contour plots for a/c = 0.20, and Sr_c = 0.150. Left column is d/c = 0.50 and right column is d/c = 2.25. **a** top, **b** middle (down), **c** bottom, and **d** middle (up) of the motion.

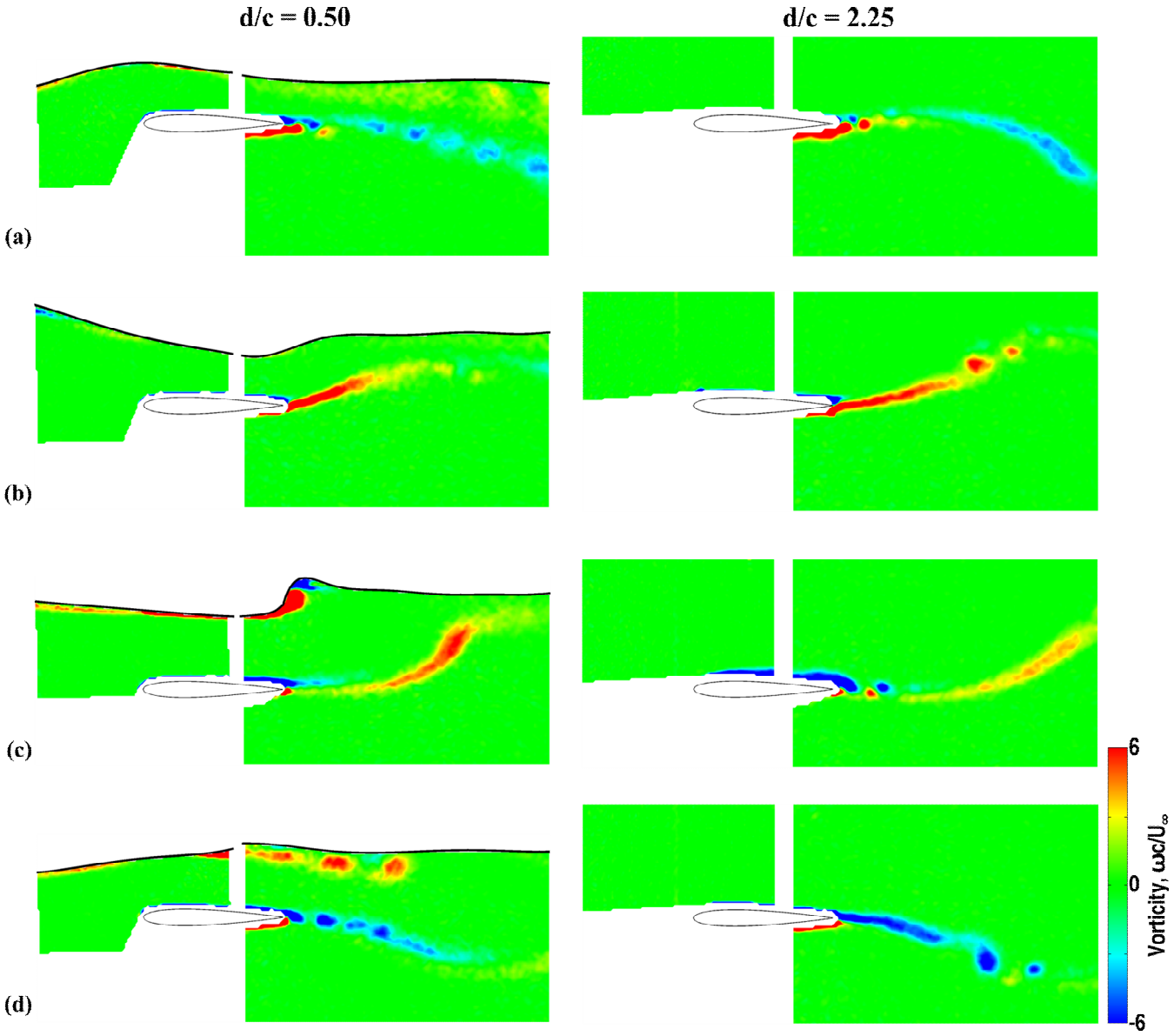

Fig. 15 Phase-averaged vorticity contour plots for a/c = 0.20, and Sr_c = 0.225. Left column is d/c = 0.50 and right column is d/c = 2.25. **a** top, **b** middle (down), **c** bottom, and **d** middle (up) of the motion.

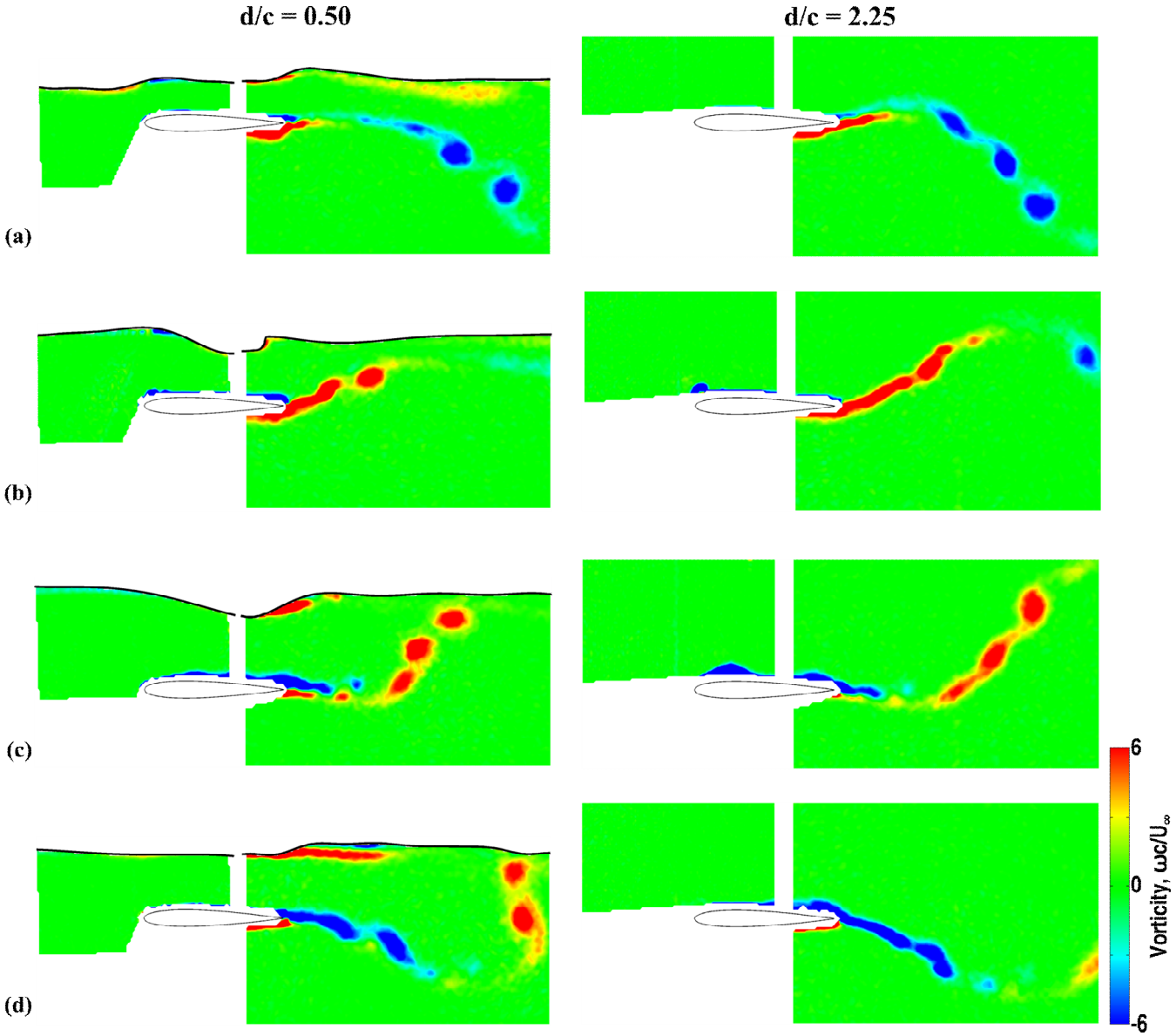

Fig. 16 Phase-averaged vorticity contour plots for a/c = 0.20, and Sr_c = 0.300. Left column is d/c = 0.50 and right column is d/c = 2.25. **a** top, **b** middle (down), **c** bottom, and **d** middle (up) of the motion.

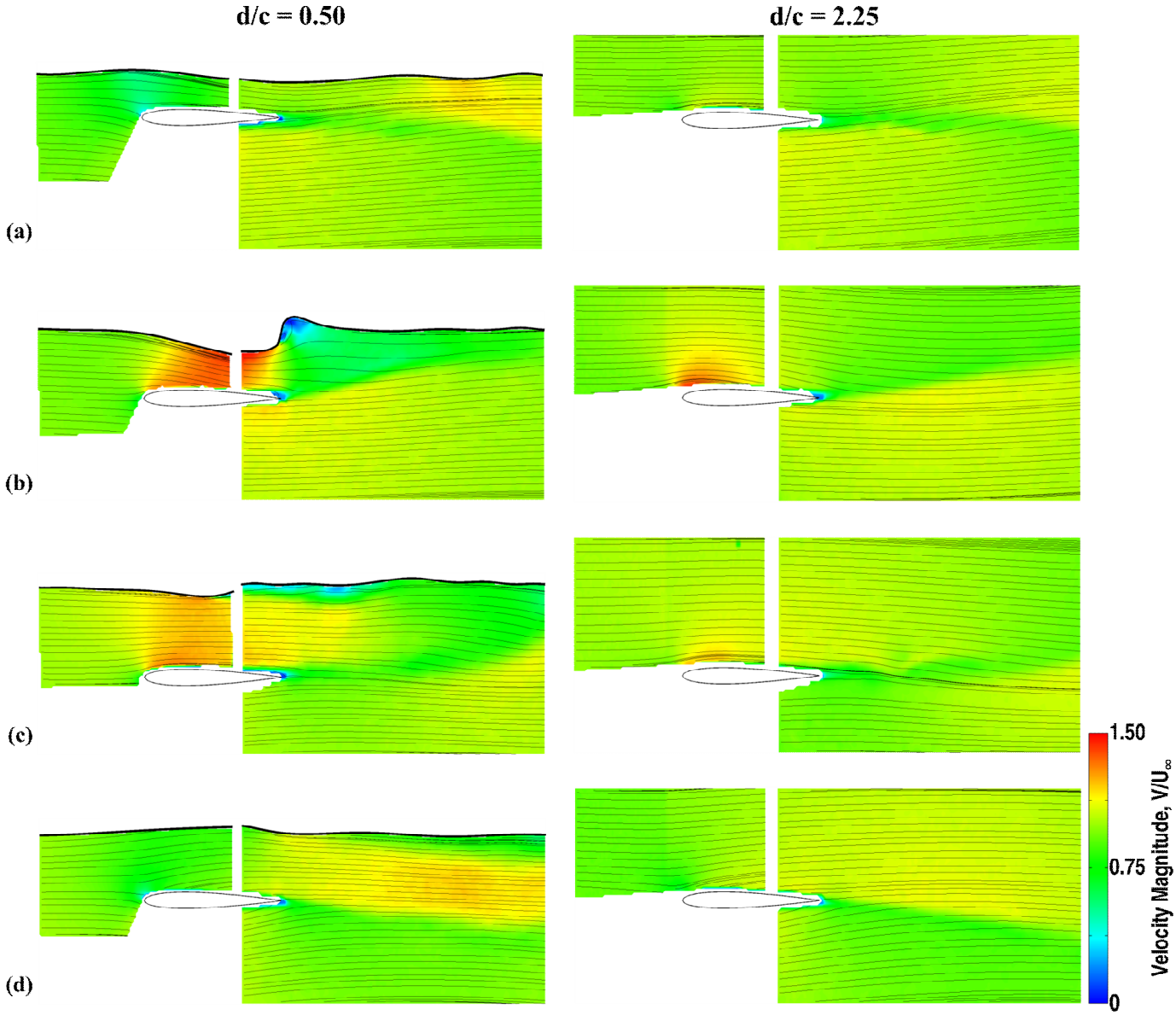

Fig. 17 Phase-averaged velocity magnitude contour plots for a/c = 0.20, and Sr_c = 0.150. Left column is d/c = 0.50 and right column is d/c = 2.25. **a** top, **b** middle (down), **c** bottom, and **d** middle (up) of the motion.

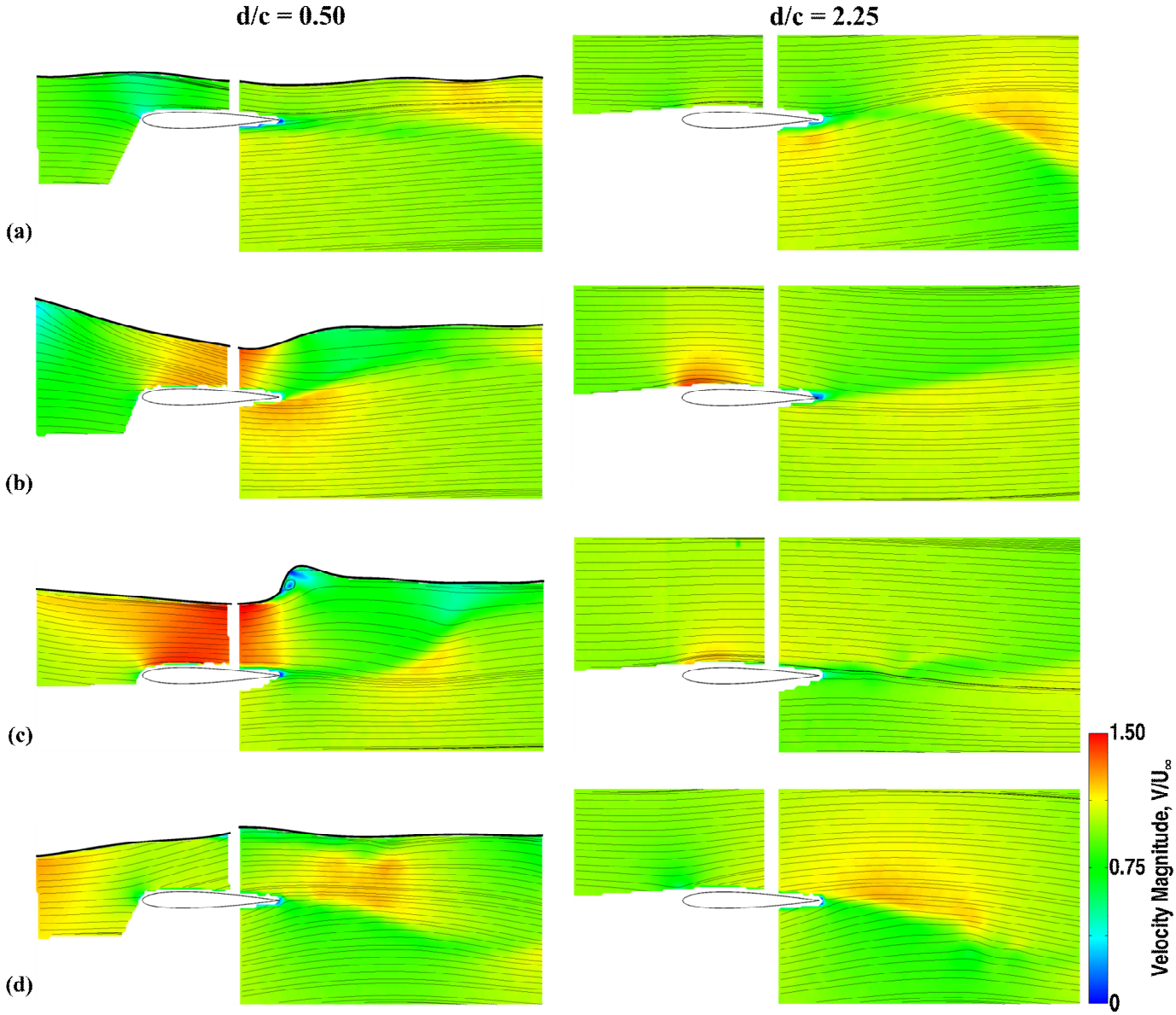

Fig. 18 Phase-averaged velocity magnitude contour plots for a/c = 0.20, and Sr_c = 0.225. Left column is d/c = 0.50 and right column is d/c = 2.25. **a** top, **b** middle (down), **c** bottom, and **d** middle (up) of the motion.

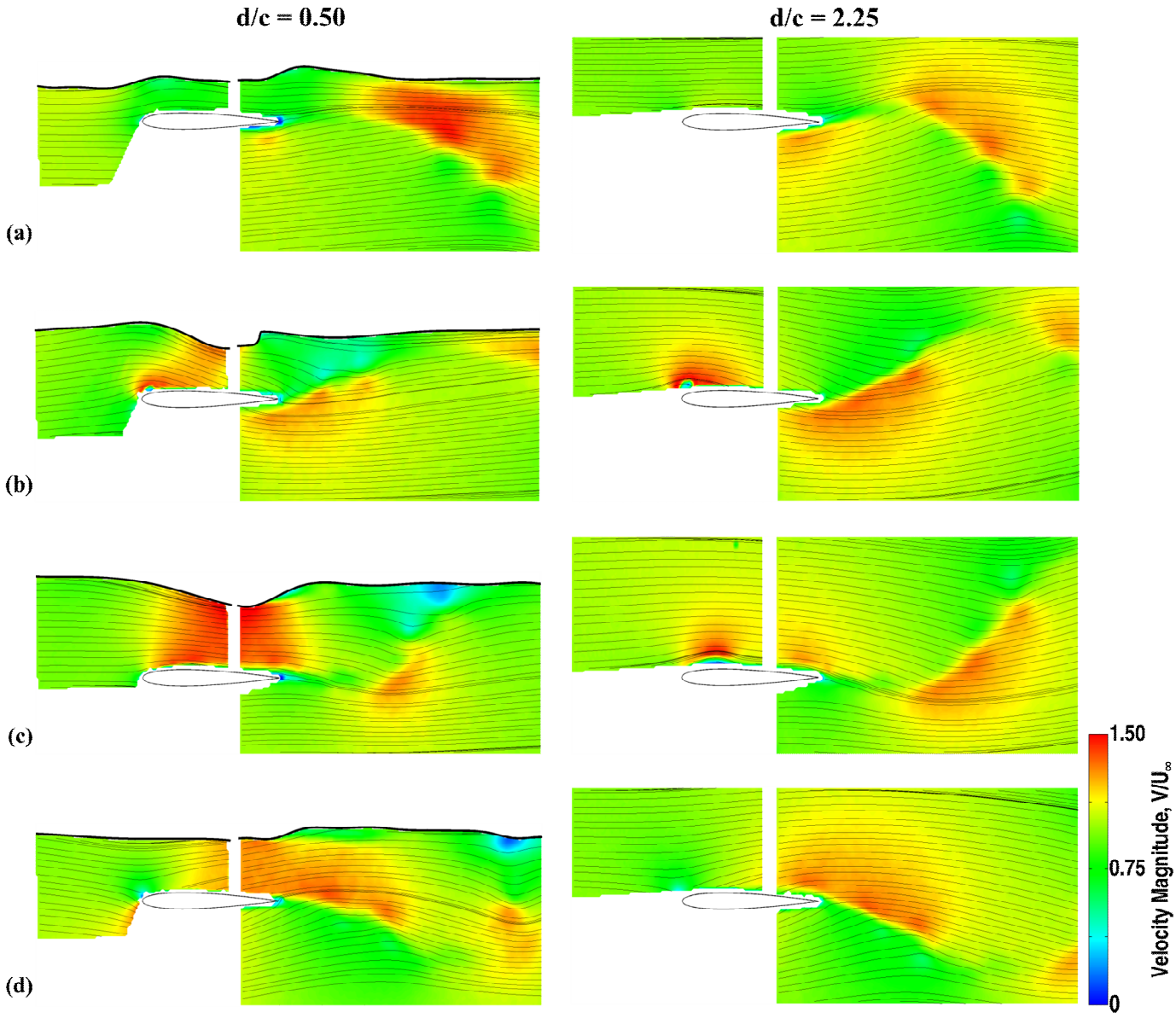

Fig. 19 Phase-averaged velocity magnitude contour plots for a/c = 0.20, and Sr_c = 0.300. Left column is d/c = 0.50 and right column is d/c = 2.25. **a** top, **b** middle (down), **c** bottom, and **d** middle (up) of the motion.